

Eccentric binaries: Periastron events and tidal heating

G. Koenigsberger^{*1} and D. Estrella-Trujillo¹

Instituto de Ciencias Físicas, Universidad Nacional Autónoma de México, Ave. Universidad S/N, Chamilpa, Cuernavaca, México
e-mail: gloria@icf.unam.mx, dtrujillo@icf.unam.mx

August 2023

ABSTRACT

Context. Binary stars cannot be fully understood without assessing the interaction effects between the two components and the impact of these effects on observational diagnostics. Periastron brightening events, also known as the heartbeat phenomenon, are a clear manifestation of this type of interaction.

Aims. We aim to explore the role of tidal shear energy dissipation in stars undergoing periastron brightening events.

Methods. We performed a computation from first principles that uses a quasi-hydrodynamic Lagrangian scheme to simultaneously solve the orbital motion and the equations of motion of a 3D grid of volume elements covering the inner, rigidly rotating "core" of a rotating, tidally perturbed star. The equations of motion include the gravitational acceleration of both stars, the centrifugal, Coriolis, gas pressure accelerations, and viscous coupling between volume elements. The method is illustrated for a grid of model binary systems with a $10 M_{\odot}$ primary that is perturbed by a $6.97 M_{\odot}$ companion in eccentric orbits ($e=0 - 0.7$). The model was then applied to the heartbeat star MACHO 80.7443.1718.

Results. We find an increase by factors $\sim 10^{-6} - 10^{-3}$ in tidal shear energy dissipation at periastron, consistent with the majority of observed heartbeat stars. The magnitude of the periastron effect correlates with the degree of departure from synchronicity: stars rotating much faster or much slower than the synchronous rate at periastron present the strongest effect. We confirm that for eccentricities ≤ 0.3 , pseudo-synchronization occurs for $0.8 < \omega/\Omega_{ave} < 1$, where Ω_{ave} is the average orbital angular velocity. The minimum energy rotation rate (pseudo-synchronization) for $e=0.5$ and 0.7 occurs for $1.0 < \omega/\Omega_{ave} < 1.15$. The tidal shear energy dissipation model reproduces from first principles the $\sim 23\%$ maximum brightness enhancement at periastron of MACHO 80.7443.1718.

Conclusions. Our results suggest that the magnitude and shape of the heartbeat signal may serve as diagnostics for the internal stellar rotation and turbulent viscosity values.

1. Introduction

A growing number of binary systems have been reported to undergo periastron events, that is, a change in the observable properties around the time of periastron, such as a brightness enhancement, an increase in surface activity, and/or a triggering of oscillations. Early examples include Hutchings (1979), who cited a significant increase in mass-loss rates around periastron in the two B-type systems, HD 187399 and AZ Cas, and in HD 163181 (B0Ia+0), and van Genderen & Sterken (2007) at periastron in six systems, including η Carinae.

More recently, photometric observations obtained with the *Kepler* space telescope have led to the discovery of objects that not only display periastron-related brightness enhancements, but also low-amplitude sinusoidal oscillations that tend to have frequencies that are harmonics of the orbital frequency (Thompson et al. 2012; Fuller 2017; Guo 2020). These objects have come to be known as heartbeat stars, and more than 180 are known from *Kepler* alone (Hambleton et al. 2013; Kirk et al. 2016) and many more from *BRITE* (Pigulski 2018), *ASAS-SN* (Jayasinghe et al. 2020), and *TESS* (Kołaczek-Szymański et al. 2021). These stars are all considered to be eccentric orbit binary systems with typical photometric variations $\Delta L/L \leq 10^{-3}$.

Although a large majority of the heartbeat stars have masses in the range of A-type and F-type stars, similar properties are also reported in high-mass OB-type objects such as ι Orionis (Pablo et al. 2017) and η Carinae (Richardson et al. 2018) in the Milky Way, MACHO 80.7443.1718 (Jayasinghe et al. 2019) in the Large Mag-

ellanic Cloud, and the massive multiple system HD 5980 (Sterken & Breysacher 1997; Kołaczek-Szymański et al. 2021) in the Small Magellanic Cloud. This large diversity points to a common physical mechanism which is now widely accepted to be the variable gravitational perturbation caused by the binary companion.¹

A companion distorts a star's intrinsic spherical shape producing two tidal lobes, one facing the companion and one in the opposite hemisphere. The extension of the tidal lobes is not necessarily the same on both sides and their orientation is not necessarily parallel to the line joining the stars' centers. These depend on the orbital separation as well as the star's radius, its rotation velocity, and the viscosity of its material.

In binary systems with circular orbits, the shape of the distorted stars remains approximately constant throughout the orbital cycle. However, because the viewing angle to the deformed star changes with orbital phase, the changing projected size of the disk in the sky leads to brightness variations. This so-called ellipsoidal effect is a purely geometric effect, and can be modeled using an appropriate stellar atmosphere model (Orosz & Hauschildt 2000).

Eccentric binaries differ from circular orbit systems in that the orientation of the tidal bulges with respect to the line joining the two stellar centers varies over the orbital cycle, as does their extension. These variations occur most rapidly around pe-

¹ It must be noted that periastron brightening in massive stars is often interpreted in terms of colliding winds, a phenomenon that is however hard-pressed to explain low-amplitude high-frequency post-periastron oscillations.

* Visiting scholar, Astronomy Department, Indiana University

riastron, triggering high frequency dynamical effects that show up as low-amplitude photometric variations.

Press & Teukolsky (1977) presented a mathematical framework to model the tidal distortions based on a linear superposition of the non-radial pressure and gravity mode oscillations, a framework further developed by Kumar et al. (1995) and Lai (1997), predicting the brightening around periastron and the appearance of tidally excited oscillations (TEOs) that are harmonics of the orbital period. Recent advances were achieved by Fuller (2017) to account for rotation, incorporate nonadiabatic effects, and allow for spin-orbit misalignment; Schenk et al. (2001) who studied the nonlinear interaction of modes in rotating Newtonian stars; and by Dewberry & Wu (2024) who proposed an alternative approach to the treatment of tidally driven oscillations damping that accounts for dissipative mode coupling.

As with any theoretical framework, the linear mode-decomposition models have limitations. As pointed out by Press & Teukolsky (1977), a linear mode calculation is valid if nonlinear effects are very small. Specifically, with R_1 the stellar radius and r_{per} the periastron distance, they point out that the validity of a linear mode calculation is to be doubted if $(R_1/r_{per})^2 \geq 0.10$. Indeed, using a 3D non-perturbative modeling method, Fellay et al. (2024) show that the linear approach underestimates tidal interactions by up to 40% for binary stars with small separations. In addition, the tidal interaction imposes a large-scale differential-rotation structure as well as induced oscillatory shearing motions on orbital timescales (Koenigsberger et al. 2021). An important consequence of the differential rotation is that the shearing motions can be damped through the presence of turbulent viscosity, thus converting kinetic energy into heat in a process known as tidal shear energy dissipation. However, although observational evidence exists for deviations from an adiabatic approximation (Guo et al. 2020), with a few exceptions (see, for example, Baruteau & Rieutord (2013); Astoul et al. (2021)) the current analytical models assume a rigidly rotating star and thus neglect tidal shear energy heating. Injection of this added heat into a star's subphotospheric layers causes it to expand and become more luminous, at least in the case of a solar-type star (Estrella-Trujillo et al. 2023).

In the presence of turbulent viscosity, kinetic energy in the tidal flows is converted into heat at all orbital phases, not only at periastron. However, as the star approaches and recedes from periastron, the shearing layers undergo rapid velocity variations leading to a more abrupt release of energy. Moreno et al. (2011) investigated the potential role of tidal heating as a source of periastron brightening events, concluding that it could play a significant role in this phenomenon. However, they were unable to provide quantitative constraints for three reasons. The first is that the study was limited to a single surface layer, thus neglecting the effects of underlying layers. The second is that the model needed as input a turbulent viscosity, values of which are highly uncertain. The third reason is that the viscosity remained constant throughout the calculation, whereas in reality turbulent viscosity is non-isotropic and time variable. These three limitations have now been overcome (Koenigsberger et al. 2021; Estrella-Trujillo et al. 2023) enabling this study.

The objective of this paper is to show the general features associated with tidal shear energy dissipation in eccentric binary systems, particularly the increased brightness predicted to occur around the time of periastron. The method is summarized in Section 2. In Section 3 we present the results from a grid of model calculations for a grid of binary systems having a range of orbital eccentricities and rotation velocities. In Section 4 we apply the model to one of the most extreme heartbeat stars found to date,

MACHO 80.7443.1718, and illustrate the manner in which our calculation from first principles directly predicts the observed variability amplitude. A discussion and the conclusions are presented in Section 5.

2. Method

Binary stars are defined to be in equilibrium when the orbit is circular, the rotation axis coincides with the orbital angular velocity vector, and the rotation period is equal to the orbital period. A departure from any of these conditions induces deformations of the stellar surface and excites oscillations.

Classical tidal theory divides the analytical treatment of the perturbations into the equilibrium tide model (Darwin 1880; Alexander 1973; Hut 1981, 1982) and the dynamical tide model (Zahn 1975; McMillan et al. 1987; Goldreich & Nicholson 1989; Lai 1997; Savonije et al. 1995). The first analyzes the large-scale distortion imposed by the external gravitational perturber. It assumes that the viscosity of the material leads to a lag between the principal axis of the deformed spheroid and the line of centers of the two stars. This lag is responsible for the torque that over time synchronizes the rotation and circularizes the orbit, and it is caused by the fact that the stellar material is not inviscid. The second model treats the star as an oscillator with a number of modes that are excited by the gravitational potential of the companion, and assumes that the dissipation of these oscillations is responsible for the eventual synchronization and circularization of the orbit (Ogilvie 2014 and references therein). As noted by Eggleton et al. (1998), rather than competing, each model provides a useful description of the interaction under different regimes; that is, for different masses and radii, orbital separations and eccentricities, and rotation rates. However, both models suffer from important uncertainties in the treatment of dissipation (Ogilvie 2014; Mathis et al. 2016; Barker & Astoul 2021; Terquem 2021; Townsend & Sun 2023; Sun et al. 2023). Both models are intended for studying the long term evolution of the stellar rotation and orbital properties of binary stars, with a focus on determining the timescales over which an equilibrium configuration is reached. However, the uncertainty in the dissipation limits the possibility of quantitative results.

The approach used in this paper differs significantly from the two classical models. It makes no a priori assumptions other than that the damping mechanism can be associated with the viscous stresses suffered by fluid parcels that are in relative motion with respect to each other. Such relative motions naturally occur throughout the star given the non-isotropic dependence of the tidal forcing in the radial and horizontal directions. Thus, our method relies on a viscosity parameter as it appears in the shear part of the kinematic stress tensor (e.g., Symon (1971)). The aim is to analyze the short term (orbital timescales) variations induced by the tidal interaction in order to allow a direct comparison with observational data.

The method is a computation from first principles which is named TIDES². It uses a quasi-hydrodynamic Lagrangian scheme which simultaneously solves the orbital motion of the companion and the equations of motion of a grid of volume elements covering the inner, rigidly rotating "core" of the tidally perturbed primary star. The core is defined as the interior region that is rotating as a solid body and does not necessarily coincide

² The *Tidal Interactions with Dissipation of Energy due to Shear* code in all its versions is available upon request to G. Koenigsberger and is easily implemented in any operating system running a Fortran or GNU Fortran compiler

with the nuclear burning region. The equations of motion include the gravitational acceleration of both stars as well as centrifugal, Coriolis, and gas pressure accelerations. The motions of individual elements are coupled to those of neighboring elements and to the core through viscous stresses.

The numerical scheme was first applied to the B-type system ι Orionis (Moreno & Koenigsberger 1999). It predicted a rapid increase in the stellar radius around periastron as well as small-amplitude, short-timescale oscillations throughout the orbit. It was subsequently used to produce synthetic absorption line profiles as a function of the orbital phase in ϵ Persei (Moreno et al. 2005) and α Virginis (Harrington et al. 2009; 2014; Palate et al. 2013b) and other systems (Palate et al. 2013b). The simulated line-profile variability captures many of the characteristics of the observations, namely, the spectroscopic equivalent of the ellipsoidal effects and the traveling “bumps” that are characteristic of tidally induced non-radial pulsators. The method was also used to derive the synchronization timescales for eccentric binaries (Toledano et al. 2007; Moreno et al. 2011), finding good agreement with the expression given by Zahn (2008) (his Eq. 2.5) for viscous dissipation for circular and $e=0.1$ orbits, the cited range of applicability.

The above calculations were performed for a single surface layer contiguous to the rigidly rotating internal region. The output includes the tidal perturbations in the radial and azimuthal directions and it was shown that the tidal velocity in the radial direction, v_r , is generally an order of magnitude smaller than that in the azimuthal direction, v_ϕ , consistent with the analytical results for the equatorial latitudes³ of Scharlemann (1981), derived by assuming small departures from corotation. The dominance of the azimuthal component of the tidal flows was also found by Lee (2017). This original version of the numerical method is named *TIDES-1*. It requires a viscosity value as input and its output includes the radial and azimuthal velocities for the surface layer. These velocities on the hemisphere facing the observer are then projected onto the line of sight allowing the computation of the orbital phase-dependent profile variability of photospheric absorption line profiles (Moreno et al. 2005).

The extension of the TIDES method to n layers (TIDES- n) was introduced in Koenigsberger et al. (2021) where, for circular-orbits, it was shown that the rotation rate tends toward a uniform rotation structure when synchronization is attained. However, the synchronization timescale is different for each layer, because it goes as the viscous timescale, $\sim \nu/r^2$, where ν is the viscosity and r is the radius of the particular layer. The calculation in Koenigsberger et al. (2021) showed how each layer proceeds toward synchronization and that the average angular velocity of the surface layer (at the equator) is the first to reach synchronicity, in agreement with the conclusion reached analytically by Goldreich & Nicholson (1989). TIDES- n requires a turbulent viscosity value as input. It is isotropic and remains constant throughout the calculation.

The primary results presented in this paper use the latest version of the code (TIDES-nv). It is based on the same algorithm as TIDES- n but has the additional capability of computing a turbulent viscosity at each grid point (Estrella-Trujillo et al. 2023). It outputs the azimuthal velocity, turbulent viscosity and corresponding energy dissipation rate. These variables are all non-isotropic and time-variable.

³ The inviscid approximation leads to poorer results for the tidal amplitude at latitudes closer to the poles because it neglects angular momentum to these regions from the strongly perturbed equatorial latitudes, see Harrington et al. (2009), Fig. 7.

The strongest approximation in our calculation concerns the mathematical formulation for the turbulent viscosity. Turbulent viscosity arises in unstable flows that are characterized as turbulent. Mathis et al. (2004) noted that turbulence might be expected even in stellar radiative zones due to nonlinear processes that appear at large Reynolds numbers. Understanding turbulent viscosity is a complex problem that falls in the realm of fluid dynamics and turbulent transport (see, for example, Le Bars et al. (2022); Zahn (1992); Richard & Zahn (1999); Zahn (2008); Mathis et al. (2004, 2016); Garaud & Kulenthirarajah (2016)). We use the simplest functional representation, as given by (Landau & Lifshitz 1987), in which its value is directly proportional to the instantaneous gradient in velocity of neighboring fluid parcels. This representation yields a non-isotropic and time-dependent turbulent viscosity value, which is a significantly less arbitrary approach than simply adopting a constant value. Furthermore, the viscosity thus derived includes both the shear due to the global differential rotation and the shear due to the tidally excited oscillations.

The need for a turbulent viscosity in massive star models follows from the fact that rotation induced shear is required to account for the enhanced abundances of nuclear-processed elements on the surface of main sequence massive stars (Maeder & Meynet 1996; Talon et al. 1997; Maeder & Meynet 2000). The fluid velocity used in these formulations is associated with meridional circulation currents and the differential effect of the Coriolis force (Hirschi & Maeder 2010). In binary stars with asynchronous rotation, the tidal perturbations can induce significantly larger fluid velocities and velocity gradients (Koenigsberger et al. 2021). Also, observational data of binary systems in clusters indicates that systems with orbital periods shorter than ~ 6 -8 days have mostly circular orbits, which means that the circularization process must occur on much shorter timescales than possible in the presence of only molecular viscosity. The circularization timescale that is usually applied in this case is as derived by Zahn (1977), with typical turbulent viscosities in the range $10^{10} \text{ cm}^2 \text{ s}^{-1}$ - $10^{13} \text{ cm}^2 \text{ s}^{-1}$ (Zahn 2008). It is also found that turbulent viscosity as estimated using arguments from the mixing length theory should have values on the order of 10^{12} - $10^{13} \text{ cm}^2/\text{s}$ (Käpylä et al. 2020).

It is interesting to note that viscosity values that are orders of magnitude larger than the molecular (kinematical) viscosities (1 - $10^3 \text{ cm}^2/\text{s}$) appear in many additional contexts. For example, numerical simulations of the solar convective region use a viscosity value 10^{10} - $10^{12} \text{ cm}^2/\text{s}$ (Elliott et al. 2000) based on the idea that the dynamics are expected to be governed principally by the largest (and most energetic) eddies, and not to be sensitive to small-scale flow features.⁴ This is in contrast to the value of kinematic viscosity $\sim 27 \text{ cm}^2/\text{s}$ at the solar center discussed in Fig. 3 of Caleo et al. (2016), where the plasma conditions are significantly different from those in the convective zone. Also, Pérez-de-Tejada (1999) estimated $\nu=6 \cdot 10^{13} \text{ cm}^2/\text{s}$ for this parameter in boundary layers around solar system planetary ionospheres; Efroimsky (2018) used the outgoing energy flux due to the vapor plumes in Saturn’s moon Enceladus to estimate that its mean tidal viscosity $\eta=\nu\rho \sim 0.24 \cdot 10^{14} \text{ Pa s}$ (which translates into $\nu \sim 2 \cdot 10^{14} \text{ cm}^2/\text{s}$ assuming a mass density $\rho \sim 0.9$ for ice); and Shi et al. (2006) found $\eta \sim 10^{19} \text{ Pa-s}$ for Earth’s crustal medium at a depth of 32 km.

⁴ Elliott et al. (2000) note, however, that the large viscosity used in their models should be regarded as an artificial viscosity whose values are chosen to suitably truncate the nonlinear energy cascade and thereby prevent nonlinear instability.

2.1. Definition of parameters

The star whose tidal perturbations are being considered is called the "primary", and its mass and unperturbed radius are denoted, respectively, m_1 and R_1 . The companion is assumed to be a point source and its mass is labeled m_2 . The primary's initial rotation is uniform and the rotation axis is perpendicular to the orbital plane. A number N_r of stellar layers are allowed to respond to the forces in the system. This leads to a departure from the initial uniform rotation structure as it evolves over time.

We characterize the initial rotation velocity in terms of the synchronicity parameter $\beta_0 = \omega_0 / \Omega_0$, where ω_0 is the initial rotation angular velocity and Ω_0 is the orbital angular velocity at a reference point. For eccentric orbits, periastron is a convenient reference point, so that β_0 can be cast in the form: $\beta_0 = 0.02P \frac{V_{rot}(1-e)^{3/2}}{R_1(1+e)^{1/2}}$. Here, P is the orbital period in days, V_{rot} is the initial equatorial rotation velocity of the uniformly rotating star (initial condition) in km/s, and R_1 is the stellar radius in solar units.

Table 1. Description of input parameters.

Parameter	Value	Description
P_{orb}	(a)	Orbital period (days)
e	(a)	Orbital eccentricity
m_1	10	Primary mass (perturbed star) (M_\odot)
m_2	6.97	Secondary mass (point source) (M_\odot)
R_1	5.48	Undisturbed primary radius (R_\odot)
β_0	(a)	Initial synchronicity parameter
λ	1	Turbulent viscosity coefficient
IND	3	Polytropic index
$\Delta R/R_1$	0.06	Layer thickness
N_r	10	Number of layers
N_φ	200	Number of partitions in longitude
N_θ	20	Number of partitions in latitude
Tol	10^{-7}	Tolerance for Runge-Kutta integration

Notes. (a) See Tables 2, 4, and 3.

Table 2. Overview of the model grid.

Set	e	P	a	N_{cy}	N_{phases}
E0.0	0.0	6.00	35.7	30, 50	10
E0.1	0.1	6.00	35.7	30, 50	10
E0.3	0.3	8.75	45.9	30, 50	130
E0.5	0.5	14.49	64.3	12, 20	130
E0.7	0.7	31.18	107.2	5, 10	169

Notes. e is the orbital eccentricity, the orbital period P is given in days, and the orbital semimajor axis a is given in R_\odot . N_{cy} is the number of orbital periods at which the results were sampled and N_{phases} is the number of orbital phases at each of the sampled cycles for which output was written.

The rate of energy dissipation per unit volume is as given in Moreno et al. (2011):

$$\dot{E}_V \simeq \nu \rho \left\{ \frac{4}{3} \left(\frac{\partial \omega}{\partial \varphi} \right)^2 + \left[r^2 \left(\frac{\partial \omega}{\partial r} \right)^2 + \left(\frac{\partial \omega}{\partial \theta} \right)^2 \right] \sin^2 \theta \right\}, \quad (1)$$

with ν the kinematical viscosity, ρ the mass density, ω the angular velocity, and r , θ , φ , respectively, the radius, latitude, and

longitude coordinates. The units of \dot{E}_V are energy per unit time per unit volume.

The viscosity is assumed to be a turbulent viscosity and is calculated at each timestep and volume element interface using the expression (Landau & Lifshitz 1987):

$$\nu_{turb} = \lambda \ell_t \Delta u_t, \quad (2)$$

where ℓ_t is the characteristic length of the largest eddies that are associated with the turbulence, here assumed to be on the order of the layer thickness, and Δu_t is the typical average velocity variation of the flow over the length ℓ_t . The variable $\lambda \in [0, 1]$ is a proportionality parameter that describes the fraction of kinetic energy transformed into thermal energy. We used $\lambda = 1$. Inspection of Eqs. 1 and 2 and numerical experiments (Estrella-Trujillo et al. 2024, in preparation) indicate that the energy dissipation rate for different values scales approximately with the value of λ and is thus straightforward to estimate for smaller values. The above prescription is applied to the interface between each volume element and its neighboring elements. Thus, the non-isotropic and time-variable nature of the viscosity is incorporated in the calculation.

The density is obtained assuming a polytropic stellar structure. Each volume element of the grid contains a fixed mass of gas that obeys the ideal gas equation of state, which provides the corresponding gas pressure.

The total energy dissipation rate at particular times during the orbital cycle is:

$$\dot{E}_{tot}(t) = \int_V \dot{E}_V dV. \quad (3)$$

Another quantity that is of interest, especially when comparing with investigations of tidal theory, is the energy dissipation rate averaged over the orbital cycle:

$$\langle \dot{E}_{tot} \rangle = \frac{\int_0^P \dot{E}_{tot}(t) dt}{P}. \quad (4)$$

2.2. Input parameters

The TIDES input parameters are described in Table 1, where we also list the values that were kept constant. The masses and the primary star's radius were chosen to be similar to those used in Harrington et al. (2009), Harrington et al. (2016), and Koenigsberger et al. (2021). The eccentricities ($e=0, 0.1, 0.3, 0.5, 0.7$) were chosen to sample the range observed in heartbeat stars reported by Kolaczek-Szymanski et al. (2021). The orbital periods were chosen so as to keep the periastron distance at an approximately constant value, $r_{per} = 32.1 R_\odot$. The synchronicity parameters $\beta_0 = 0.2 - 1.95$ were chosen to sample the range in values of the eclipsing binaries studied by Lurie et al. (2017) (their Fig. 7)⁵

Table 2 provides an overview of the parameters that were held constant for each eccentricity set: Orbital period P, orbital semi-major axis a , number of orbital periods and phases that were sampled, N_{cy} and N_{phases} , respectively. Detailed descriptions for each model are provided in Table 3 for the eccentric

⁵ It is important to note that the rotation velocities quoted in Lurie et al. (2017) were determined based on the assumption that the light variations are caused by starspots.

orbit models and Table 4 for the circular orbit models. Column 1 lists the model number, column 2 the value of β_0 and column 3 the surface equatorial rotation velocity. This velocity corresponds to the initial equatorial rotation velocity of the uniformly rotating star.

3. Results

An initial uniform rotation state transitions into one in which the average rotation rate of each layer is either faster (if $\beta_0 < 1$) or slower (if $\beta_0 > 1$) than the initial rate (Koenigsberger et al. 2021). In all cases, the surface layer changes its velocity faster than any of the other layers. As a result, the average angular rotation is a function of distance from the stellar center. Furthermore, because the equatorial latitude is the one most strongly affected by the tidal force, it slows down or speeds up (depending on the β_0 value) faster than the polar regions. Thus, there is also an average differential rotation structure in the polar direction. Both of these differential rotation structures contribute to the total energy dissipation rate when a turbulent viscosity is present. In addition, the models rapidly develop the tidal bulges with the corresponding inflow and outflow of material. This relative motion of different mass parcels also contribute to the total energy dissipation rate.

3.1. Pseudosynchronicity

The energy dissipation rate averaged over an orbital period $\langle \dot{E}_{tot} \rangle$ is listed in Table 3 (column 3), as are the instantaneous energy dissipation rates \dot{E}_{tot} at periastron (column 4) and apastron (column 5). This table clearly shows that larger departures from synchronicity lead to larger $\langle \dot{E}_{tot} \rangle$ values. As shown in Fig. 1, minimum dissipation rates occur near the synchronization rotation rate $\beta_0 \simeq 1$ but, except for $e=0$, the actual minimum does not occur at $\beta_0=1$ but at the pseudosynchronous rate, β_{ps} , as shown analytically by Hut (1981). However, contrary to the analytical result which predicts a relatively constant β_{ps} value for $e \geq 0.2$, our β_{ps} values depend on eccentricity. Another difference is that although the analytical result predicts a unique $\beta_{ps} < 1$ value for the minimum energy rotation state, our $e=0.5$ and 0.7 models show a flat and extended minimum at $\beta_0 > 1$. A similar result was found by Moreno et al. (2011) based on denser β_0 grids. The flat minimum is also consistent with the recent finding of a blurred pseudosynchronization in numerical calculations of the high eccentricity binary KOI-54 (Townsend & Sun 2023).

A bifurcation between subsynchronous and supersynchronous rotation is present in the perturbed rotation velocity. This is quantified by finding the maximum/minimum angular velocity at each latitude and layer depth, and is defined as $\pm|\omega_{max}|$. That is, the value of the maximum departure from the rest frame velocity, with the sign indicating whether it is in the direction of rotation (positive sign) or in the opposite direction. In the subsynchronous rotators, $|\omega_{max}| > 0$, as expected since the action of the tidal force is to accelerate the stellar rotation toward corotation. The opposite is true for the supersynchronous rotators. Examples of this behavior for the surface layer at the equator are shown in Figs. A.1 and A.2. These show that when rotation is close to the pseudosynchronous rate, $|\omega_{max}|$ displays high frequency oscillations in addition to the rapid excursions to either large positive or negative values around periastron. For systems with circular orbits, the energy dissipation rate decreases symmetrically around $\beta_0=1$, tending toward a null value at synchronicity as expected (Table 4).

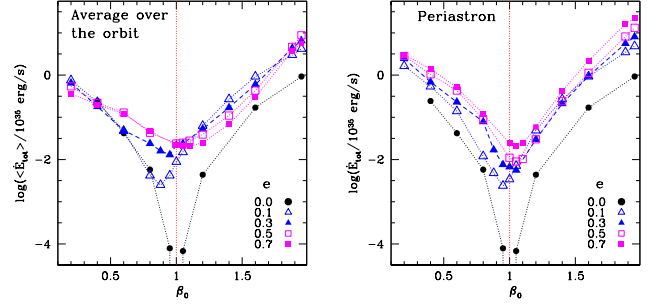


Fig. 1. Energy dissipation rate as a function of the degree of synchronicity β_0 . Colors correspond to the eccentricity of the model, as indicated in the legend. *Left:* Average over an orbital cycle, $\langle \dot{E}_{tot} \rangle$. *Right:* Value at periastron, \dot{E}_{tot}^{per} . The vertical line indicates $\beta_0=1$, corresponding to the synchronous rotation rate for a circular orbit system.

3.2. Orbital phase-dependence and periastron events

Fig. 2 illustrates the orbital phase-dependent behavior of \dot{E}_{tot} in the $e=0.3$ models. Several trends are clearly visible: a) there is always an increase in \dot{E}_{tot} around the time of periastron; b) maximum intensity tends to occur shortly after periastron; c) the durations of the periastron event is shorter in the subsynchronous models than in the supersynchronous models; d) models with $|\beta_0 - 1| \simeq 1$ present a dip at periastron; and e) models with $|\beta_0 - 1| \simeq 1$ display high frequency oscillations. The orbital phase-dependent behavior for $e=0.5$ and $e=0.7$ is similar to that of $e=0.3$, as shown in Fig. 3, but the amplitude of the rise in brightness around periastron increases with increasing eccentricity.

Assuming that the primary star in our models is similar to the B-type star in the *Spica* system, we can adopt $L_* = 4 \cdot 10^{37}$ ergs/s (Tkachenko et al. 2016) and compare the brightness enhancements at periastron due to tidal shear energy dissipation to this luminosity. We list in Column 6 of Table 3 the difference between the maximum around periastron and the mean value at apastron normalized to L_* : $\Delta \dot{E}_{tot}/L_* = (\dot{E}_{tot}^{per} - \dot{E}_{tot}^{ap})/L_*$. We find values mostly in the range 10^{-5} to 10^{-3} , with a few as low as 10^{-6} and others as high as 10^{-2} , the latter in models with the highest rotation rates and largest eccentricity. Values in the range 10^{-6} - 10^{-3} are typically found in the heartbeat stars.

A curious feature in Column 6 of Table 3 is that some of the values of $\Delta \dot{E}_{tot}/L_*$ are negative. This is because of the dip at periastron which, in models with $|\beta_0 - 1| \simeq 1$ can have a lower energy around apastron than the value of the mean.

The value of viscosity ν_{turb} plays a crucial role in determining the energy dissipation rate. Our results confirm the idea that ν_{turb} has a time-dependence in addition to a dependence on spatial coordinates. For example, we find ν in the range 10^{12} cm²/s - 10^{15} cm²/s for the inner and surface layers, respectively (see Table A.1) at periastron and smaller values around apastron.

The turbulent viscosities we derive for inner layers are on the order of those found by Penev et al. (2007) and others (Zahn 2008) 10^{10} - 10^{13} cm²/s, but the surface values are likely to be overestimates, an issue that could be resolved with a variable λ value if a straightforward theoretical formulation existed for predicting the rate of conversion from the tidal kinetic energy into heat. This remains an open question.

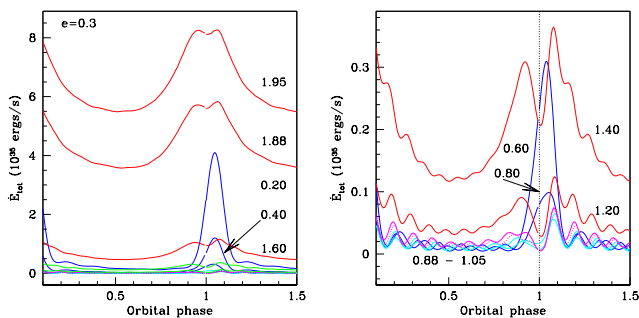


Fig. 2. Total energy dissipation rate (in units of 10^{35} ergs/s) as a function of the orbital phase for the $e=0.3$ set of models. Models with $\beta_0 < 0.80$ (blue) show a relatively narrow periastron effect with a single peak centered in phase slightly after periastron passage. Models with $\beta_0 \geq 1.20$ show a significantly broader periastron effect with a structured peak. Models with $1.20 \leq \beta_0 < 0.80$ tend to have a dominant peak after periastron and multiple weaker peaks at other phases. *Left:* All models of the set; *Right:* Models with $0.60 \leq \beta_0 \leq 1.40$, which have the weakest energy dissipation rates and are plotted on a scale that shows the variations associated with the tidally excited oscillations.

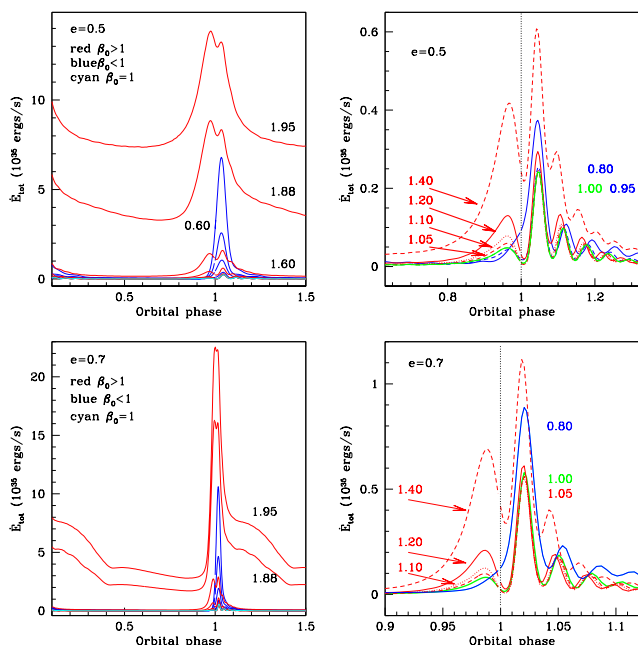


Fig. 3. Total energy dissipation rate (in units of 10^{35} ergs/s) as a function of the orbital phase for the $e=0.5$ (top) and $e=0.7$ (bottom) models. All β_0 values modeled are plotted on the left while on the right we zoom in on the $0.80 \leq \beta_0 \leq 1.40$ cases. Although the orbital elements are all the same in these models, the perturbation duration around periastron differs, being longer for faster rotation rates (larger β_0 values). The lowest-lying curves are those for $\beta_0=1.00$ (green), 1.05 (red dash) and 1.10 (red dot), all of which display several discrete peaks between orbital phase 0.9-1.3.

3.3. Conclusions from this section

We find that the pseudosynchronous rotation rate β_{ps} for $e=0.1$ and 0.3 is slower than the synchronous rate at periastron while that for $e=0.5$ and 0.8 is faster. Contrary to the results of Hut (1981), β_{ps} is not approximately constant for eccentricities $e > 0.2$ (see his Fig. 3, the curve labeled Ω_{ps}/n_p , which is equivalent to our β_{ps}). A possible source for this discrepancy may be the assumption of uniform rotation in Hut (1981) while our re-

sults are obtained for a star that has differential rotation. Our results are consistent with those of Moreno et al. (2011) who found that β_{ps} does not have a unique value for $e=0.5$ and 0.7 but that the minimum energy state occurs for a range of rotation rates near the synchronous rate at periastron. This broad β_{ps} region is also consistent with the blurred pseudosynchronization found in the numerical calculations of Townsend & Sun (2023).

There are clear trends in the orbital phase-dependent behavior of the energy dissipation rates visible in all eccentricities that we modeled: a) maximum brightness tends to occur slightly after periastron, not at periastron; b) the duration over which an increased brightness may be observed is shorter in the subsynchronous models than in the supersynchronous models; c) for fixed values of orbital period and eccentricity, the energy dissipation rate increases with increasing departure from synchronicity, with the largest values found for $\beta_0 \gg 1$; d) for fixed values of β_0 and periastron distance, the energy dissipation rate increases with increasing eccentricity; e) models with $|\beta_0 - 1| \approx 1$ present a dip in brightness at periastron as well as prominent high frequency variations that we identify with tidally excited oscillations.

4. Modeling the heartbeat star MACHO 80.7443.1718

MACHO 80.7443.1718 is located in the Large Magellanic Cloud Lucke-Hodge 58 association, which contains stars formed within the past few million years (Garmany et al. 1994). It was classified as an eclipsing binary system (Alcock et al. 1997) and has recently been found to display a $\sim 40\%$ peak-to-peak variability amplitude with morphology that places it among the heartbeat-type stars (Jayasinghe et al. 2019). An analysis of the light curve and radial velocity curve of photospheric absorption lines was performed by Jayasinghe et al. (2021), leading to the conclusion that minimum light coincides with the time of periastron passage, defined to occur at orbital phase $\varphi=0$, and maximum light at $\varphi \sim 0.04$. The times of minima in the light curve were found to undergo a systematic change by 11.1 s/yr (Kotaczek-Szymański et al. 2022). If interpreted to represent times of central eclipse, this implies an extraordinarily large rate of change in the orbital period.

The observed brightness increase $\Delta F/F \sim 23\%$ at periastron far exceeds the typical values in the range $10^{-6} - 10^{-3}$ usually found in heartbeat stars (Fuller 2017). MacLeod & Loeb (2023) pointed out that the stellar radius of $24 R_\odot$ deduced from the spectroscopic observations (Jayasinghe et al. 2021) was inconsistent with the significantly larger tidal distortion needed by standard theories to explain such strong light curve variations. In order to address this problem, MacLeod & Loeb (2023) performed a hydrodynamic simulation that predicts a tidal wave raised at periastron having an extension of several solar radii, and concluded that the breaking wave could lead to shock-heating on the surface of the star. These results, however, are based on several assumptions, the strongest of which is that the core of the primary star is excised from the calculation and treated as a point mass leaving the envelope detached from the core. In addition, both the radius and orbital eccentricity are overestimated to obtain the desired result.

In the previous sections, we showed that tidal shear energy dissipation can play an important role in describing the heartbeat-star phenomenon. In this section we present results from applying the model to MACHO 80.7443.1718.

4.1. Brightness variations from tidal heating

We computed a TIDES-nvv model for MACHO 80.7443.1718 using as input the values that were obtained by Jayasinghe et al. (2021) from their analysis of the observational data. Table 5 lists these input parameters. The projected rotation velocity deduced from the widths of the photospheric absorption lines is 174 km/s which, with an assumed orbital inclination of 44° , implies an equatorial rotation velocity $V_{rot}=250$ km/s. This yields $\beta_0=1.95$. The range in V_{rot} values implied by the measurement uncertainties in $V\sin(i)$ quoted by Jayasinghe et al. (2021) corresponds to a range $\beta_0=1.57$ -2.34. Hence, the primary star of the system is in supersynchronous rotation for all possible V_{rot} values. We adopt $\beta_0=1.95$ for the calculation, which means that at apastron it is even more highly supersynchronous, $\beta_{ap}=18.2$. We used the same computational parameters as in Table 1 except for the number of layers that we set to $N_r=5$ since the largest tidal shear energy dissipation rates occur in the surface layers. The model was evolved out to 100 orbital periods (9 years), with output retained at 5, 10, 20 and 50 orbital periods.

The resulting total tidal energy dissipation rate \dot{E}_{tot} at periastron and apastron is, respectively, $3.7 \cdot 10^{38}$ ergs/s and $6.6 \cdot 10^{36}$ ergs/s. The normalized light curve, obtained by adding the phase-dependent \dot{E}_{tot} to the stellar luminosity $L_* = 1.57 \cdot 10^{39}$ ergs/s cited in Jayasinghe et al. (2021) and dividing by this number, is illustrated in Fig. 4. It shows a 23% increase at maximum, with maximum occurring at orbital phase ~ 0.06 after periastron passage. The brightness increase is not symmetrical around periastron but initiates at $\varphi \sim 0.9$ and ends at $\varphi \sim 0.3$. These results are all consistent with the observations.

We emphasize that our results follow directly from a calculation performed from first principles, with no fitting to the data, no prior assumptions and no adjustable parameters other than the conversion rate of kinetic energy into heat (λ). However, several comments are in order. The n-layer, variable-viscosity version of our model provides only the tidally induced perturbations in the azimuthal direction due to computational challenges⁶ Thus, it is likely to yield an underestimate of the total energy dissipation rate. On the other hand, the value of λ we have used is the upper limit of this parameter and is certainly an overestimate. Adding in the energy dissipation rate associated with the radial perturbation components might counterbalance the use of a smaller, more realistic λ value.

A final comment is in order regarding the average tidal energy dissipation rate that we find in our model which, at first sight, might seem very large in the context of the tidal evolution of the system. Using Eq. (9) of Koenigsberger & Moreno (2016) and the energy dissipation rate average over an orbit, we find $\dot{P}/P \approx 1.4 \times 10^{-3}$ s/yr. Kołaczek-Szymański et al. (2022) reported variations in the light curve that they interpret in terms of a decreasing orbital period at a rate of 11 s/yr, which would imply an energy loss from the orbit that is orders of magnitude larger than that associated with the tidal shear energy dissipation rate that we have derived.

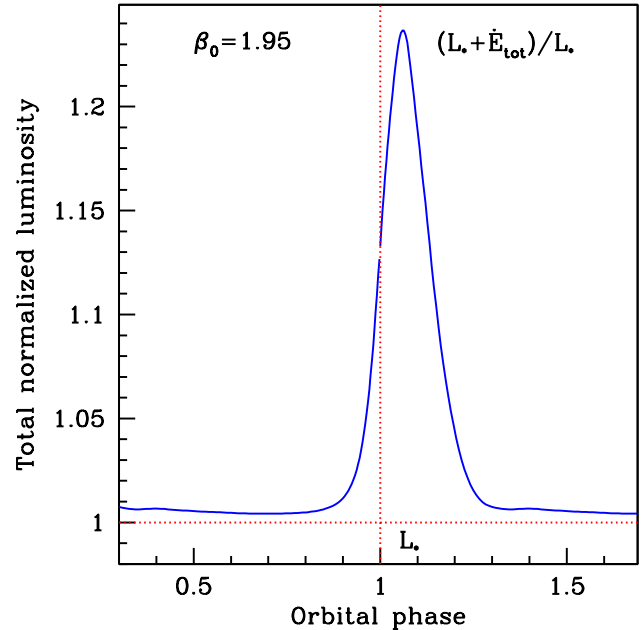


Fig. 4. Predicted MACHO 80.7443.1718 light curve from the tidal shear energy dissipation calculation added to the stellar luminosity given by J21, $L_* = 1.63 \cdot 10^{39}$ ergs/s, and normalized to this value. The vertical dotted line indicates the time of periastron and the horizontal line indicates the normalized luminosity level. Tidal shear contributes $\sim 23\%$ of the luminosity peak around the time of periastron.

4.2. Radius and perturbed radial velocity component

In order to explore the effects of the radial component of the tidal perturbation we performed two tests with a one-layer model based on the TIDES-nvv algorithm but that allows radial motions. As with the original version, in this new version (TIDES-1vv) the surface layer remains attached to the underlying rotating core at all times and is coupled to it through the viscous force. The first test was performed with $\lambda=1$, as was used with the n-layer calculation and the second with $\lambda=0.01$. For comparison, we also computed two models using the original one-layer model discussed in Moreno et al. (2005) and Moreno et al. (2011). All input parameters are the same as for the TIDES-1vv calculation except that in this case a fixed viscosity value is needed as input. We explored values $\nu=0.028 R_\odot^2/d$ ($1.6 \cdot 10^{15}$ cm²/s) and $\nu=2 R_\odot^2/d$ ($2.3 \cdot 10^{17}$ cm²/s) which are on the order of magnitude of those that were computed by TIDES-nvv with $\lambda=1$. All the calculations were performed with 500 partitions in the azimuthal direction.

We find that the primary tidal bulge at periastron extends no more than $\sim 0.13 R_\odot$ above the equilibrium radius. The four calculations yield a similar average shape (Fig. 5). The differences can be traced to the viscosity values, with smaller viscosities allowing for the appearance of high frequency oscillations in both radius and velocity.

The size of the main tidal bulge found in our calculation can be compared with the estimate (see, for example, Zahn (2008):

$$\frac{\delta R}{R_1} \approx \frac{m_1}{m_2} \left(\frac{R_1}{a} \right)^3, \quad (5)$$

where R_1 is the equilibrium radius, m_1 and m_2 the masses of the primary star and the perturber, respectively, a is the semimajor

⁶ With n-layers, the absence of a lower boundary for each layer allows vertical displacements of the volume elements that exceed their vertical extension; that is, they can become detached from each other, a condition that halts the numerical integration. A full SPH computation is required to keep track of the 3D location of each volume element and allow for buoyancy effects.

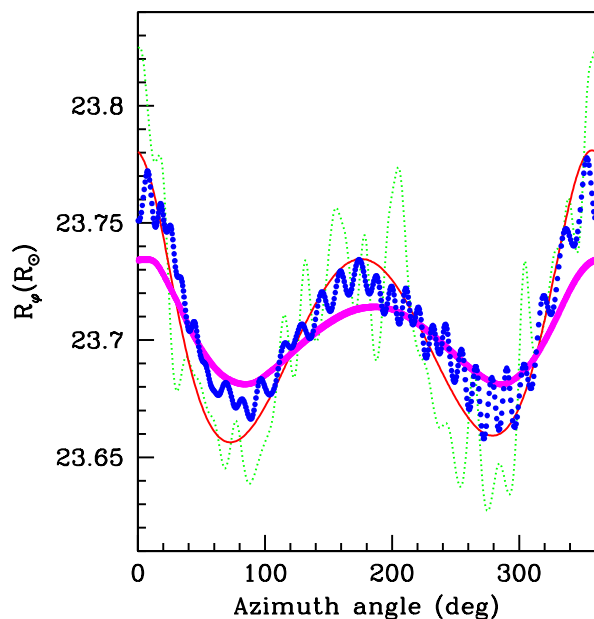


Fig. 5. Equatorial radius of MACHO 80.7443.1718 at periastron as a function of the longitude obtained with the TIDES-1 models using $\nu=0.028 R_{\odot}^2/d$ (green) and $\nu=2 R_{\odot}^2/d$ (red), and the TIDES-1vv with $\lambda=0.01$ (blue) and $\lambda=1$ (magenta). The sub-binary longitude is at $\varphi=0^\circ$. Each dot in the plot correspond to a grid point. The smaller viscosity models display 28 wave-like oscillations in the radius over the 2π radians of the stellar circumference.

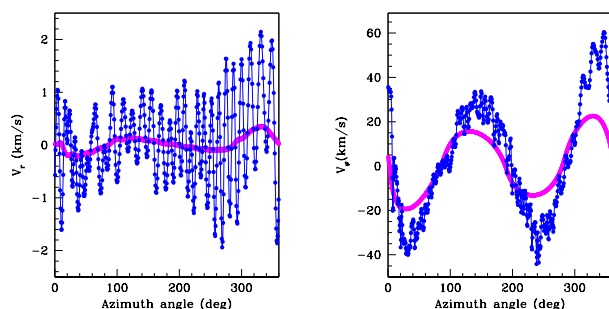


Fig. 6. Velocity in the radial direction (left) and azimuthal direction (right) along the equator of the MACHO 80.7443.1718 surface at periastron as a function of the longitude. The colors indicate results from the calculations using the code TIDES-1vv with $\lambda=0.01$ (blue); and with $\lambda=1$ (magenta). The sub-binary longitude is at $\varphi=0^\circ$. Each dot in the plot correspond to a grid point. The smaller viscosity models ($\lambda=0.1$) display wave-like velocity structures along the stellar circumference.

axis, and $\delta R = R_{bulge} - R_1$. This relation gives $\delta R \approx 0.17 R_{\odot}$, which is comparable to our maximum value $0.13 R_{\odot}$.

In general, the tidal velocity field has components in the three spatial directions. Our one-layer computations calculate the values in the radial and azimuthal directions. The two TIDES-1vv tests yield the behavior of the radial component that is shown in Fig. 6 (left). The $\lambda=0.01$ calculation displays high frequency oscillations with maximum amplitudes ~ 2 km/s at longitudes $300^\circ - 360^\circ$. Thus, our model indicates that the rise to the tidal bulge is through a series of oscillations of increasing amplitude. The azimuthal velocity component also displays high frequency oscillations which, however, have a small amplitude compared to the large-scale equilibrium tide component which reaches speeds as

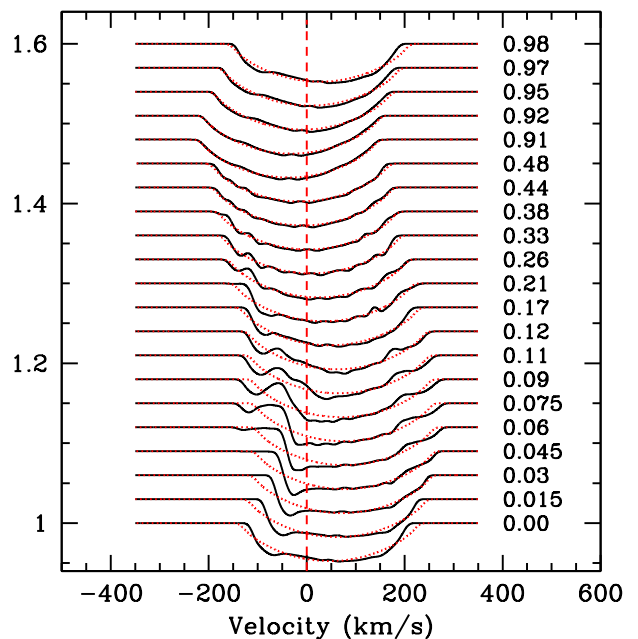


Fig. 7. Line profiles over an orbital cycle computed with the one-layer model of Moreno et al. (2005) for MACHO 80.7443.1718 assuming $\beta_0=1.95$ and the masses, radius, and orbital elements given by Jayasinghe et al. (2021). The unperturbed and rotationally broadened profiles (red dots) are superposed on the predicted profiles (black) which show significant distortions only in the orbital phase between just before periastron ($\varphi \sim 0.97$) until ~ 0.3 in phase after periastron, consistent with the duration of the luminosity increase.

high as ~ 100 km/s as it rises into the primary tidal bulge (Fig. 6 right).

The most significant difference between the one-layer calculations is the presence of high frequency oscillations in the models having smaller viscosity values. This suggests that although large λ values are needed for our results to be consistent with the observed maximum brightness, the value of this parameter needs to decrease at the surface in order to allow for TEOs, a reasonable expectation given the significantly lower density of the surface compared to inner layers, as well as its optically thinner properties allowing energy to escape. Allowing for a variable λ parameter is, however, beyond the scope of the current paper.⁷

4.3. Photospheric line profile variations

The tidal flows and radial motions excited by the tidal perturbation alter the smoothly varying rotation velocity across the stellar disk, projected onto the line of sight to the observer. Hence, instead of the typical rotationally broadened photospheric absorption line profile that would be observed if the surface were stationary in the rest frame, it appears distorted and varies over time as different portions of the stellar surface come into view. Moreno et al. (2005) incorporated the calculation of line profiles into the TIDES-1 calculation. The tidally perturbed velocities on the visible portion of the stellar disk are projected onto the line

⁷ We note that the percentage contribution from each layer of radius $r/R_{\odot}=[16.6,18.0,19.4,20.9,22.3]$ to the total energy dissipation rate at periastron is respectively [$<0.01, 0.2, 0.55, 0.2, 0.05$]. Hence, a very small λ value in the surface layer will not affect the conclusion that tidal shear energy dissipation can explain the brightness variations of MACHO 80.7443.1718 and other heartbeat stars.

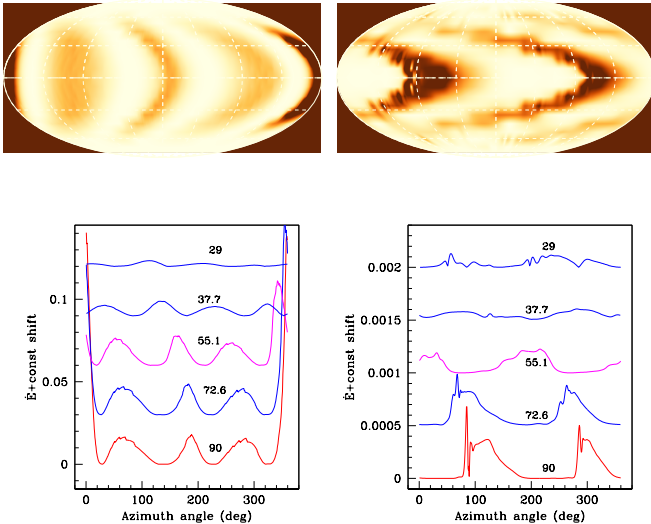


Fig. 8. Distribution of the tidal shear energy dissipation in MACHO 80.7443.1718 from the TIDES-nv model at periastron (left) and apastron (right). Top: Maps of the surface, with the sub-binary longitude at $\varphi=0^\circ$ and 360° (the rims of the maps), and the poles at the top and bottom. Dark brown represents maximum energy dissipation rate and minimum is color coded white. *Bottom:* Plots of the corresponding \dot{E} per unit volume (in units of 10^{35} ergs/s/unit volume) at various latitudes between the equator and the pole. Each curve is labeled with its corresponding colatitude angle. Each latitude is shifted vertically by 0.03 units for display purposes.

of sight to the observer. The corresponding Doppler shifts are applied to the local (on each surface element) line profile and all line profiles are added to produce the photospheric line profile that is predicted for each particular orbital phase. The method has successfully modeled the line profile variations that are observed in the eccentric B-type binary *Spica* (Harrington et al. 2009; Palate et al. 2013a; Harrington et al. 2016).

Fig. 7 is a montage of line profiles predicted by the TIDES-1 calculation using the input parameters for MACHO 80.7443.1718 in Table 5. They are stacked from bottom to top in order of increasing orbital phase and show that the strongest perturbations are expected to be observed just before periastron and until approximately 0.3 in phase after periastron. It would be interesting to determine whether similar variations are indeed present in lines that are not affected by a stellar wind, such as He I λ 4921 shown in Jayasinghe et al. (2021) but, unfortunately, the high quality spectra presented by these authors only cover the orbital phase range 0.27-0.81.

4.4. Non-isotropic energy dissipation structure

The distribution of the tidal shear energy dissipation rate over the surface is non-isotropic, and changes between periastron and apastron as shown in Fig. 8. At periastron, maximum energy is concentrated around the sub-binary longitude and extends to colatitudes as high as $\sim 60^\circ$. Three additional locations of large energy dissipation rates can be seen at approximately 90° , 180° and 270° from the sub-binary longitude. At apastron, maxima occur near 90° and 270° at the equator, however at higher latitudes maxima are spread out in long arch-like structures spanning broad ranges in longitude.

4.5. Conclusions of this section

Our n-layer calculation of the tidal shear energy dissipation rate yields a light curve with a $\sim 23\%$ maximum which occurs slightly after periastron passage, as is observed. These results follow directly from a calculation performed from first principles with no fitting to the data and no adjustable parameters other than the conversion rate of kinetic energy into heat (λ). The only basic assumption in our treatment is that relative motions excited by the tidal force gives rise to a turbulent viscosity.

We find that the maximum radial deformation of the star at periastron is $\leq 0.2 R_\odot$, contrary to the several R_\odot that was found by MacLeod & Loeb (2023), and that the radial velocity of the material rising into the primary bulge is subsonic, ~ 2 km/s, contrary to the 20 km/s found by these authors. Our results indicate that it is the horizontal velocity component that reaches supersonic velocities, attaining speeds as high as ~ 50 km/s.

The light curve does not predict the minimum that is observed at periastron. This minimum could result from a physical eclipse as suggested by MacLeod & Loeb (2023), but according to the parameters derived by Jayasinghe et al. (2021) such an eclipse would be at best a grazing eclipse. The tidal shear energy dissipation models discussed in Section 3 do predict a minimum at periastron but only in stars that are rotating close to synchronicity at this orbital phase. MACHO 80.7443.1718 is rotating at approximately twice the synchronous rate. An alternative scenario for a light curve minimum is one in which a puff of dense material is ejected at periastron. This material would dim the star until it has expanded enough to become optically thin, at which time it would become the source of emission lines such as H α and H β . MacLeod & Loeb (2023) also suggested that the activity at periastron could lead to material leaving the star.

Jayasinghe et al. (2021) detected spectral variations in MACHO 80.7443.1718 that suggest that, indeed, enhanced mass-loss episodes occur. Hence, the prominent dip in the light curve, not predicted by our tidal shear energy dissipation model, could be caused by the ejected material. We speculate that the mechanism for mass ejection may be found in the large velocity gradients around periastron combined with the rapid rise in the stellar bulge. Furthermore, similar processes are likely also present in the companion, whose contribution to the observed phenomenon should in the future be assessed.

5. Summary and conclusions

We examine the role of the often neglected process of tidal shear energy dissipation \dot{E} in shaping the observational properties of stars in which periastron brightening events occur. Our model consists of a direct calculation from first principles of the motions induced on a rotating star by a companion in an eccentric orbit. The value of \dot{E} is computed using a non-isotropic and time-dependent viscosity. We explore the impact of stellar rotation on \dot{E} in a test binary consisting of a $10 M_\odot$ primary that is perturbed by a $7 M_\odot$ companion with orbital periods in the range 6 d-31 d and eccentricities e in the range 0–0.7.

The model grid includes rotation rates at periastron that are subsynchronous ($\beta_0 < 1$), synchronous ($\beta_0 = 1$), and supersynchronous ($\beta_0 > 1$), where $\beta_0 = \omega_0 / \Omega_0$. Here, ω_0 is the rotation angular velocity of the inner, rigidly rotating region that includes the stellar core and Ω_0 is the orbital angular velocity at periastron.

We find that the shear energy dissipation rate increases by factors $\sim 10^{-6}$ – 10^{-3} at periastron, consistent with the majority of observed heartbeat stars, and we find the following trends in

\dot{E} : a) maximum \dot{E} occurs at orbital phases slightly after periastron, not at periastron; b) the timescale over which \dot{E} increases and then decreases is shorter in the subsynchronous models than in the supersynchronous models; c) for fixed values of orbital period and eccentricity, \dot{E} grows with increasing departure from $\beta_0 \sim 1$, with the largest values appearing for $\beta_0 \gg 1$; d) for fixed values of β_0 and periastron distance, models with larger eccentricity have a stronger periastron effect; e) models with $|\beta_0 - 1| \simeq 1$ have the lowest dissipation rates, present a dip at periastron, and display the relatively prominent high frequency variations that may be identified with tidally excited oscillations.

Pseudosynchronism is defined as the minimum energy rotation state in an eccentric binary. In this state, $\beta_{ps} = \omega_{ps} / \Omega_{ave}$, where ω_{ps} is the rotation angular velocity and Ω_{ave} is the average orbital angular velocity. We confirm the classical result that $0.8 < \beta_{ps} < 1.0$ for the cases with $e < 0.3$. However, in the $e = 0.5$ and 0.7 cases, we find $1.0 < \beta_{ps} < 1.15$, contrary to the results of Hut (1981) who found an approximately constant $\beta_{ps} \simeq 0.82$ for eccentricities $e > 0.2$.

In order to compare with observational results, we apply the model to the massive ($M_1 + M_2 = 34.5 + 15.7 M_\odot$, $P = 33$ d, $e = 0.5$) heartbeat star MACHO 80.7443.1718 which displays an unusually large ($\sim 23\%$) brightness increase at periastron. Our model directly predicts a $\sim 23\%$ increase in tidal shear energy dissipation rates at periastron. It thus accounts in a straightforward manner for the extraordinarily large brightness increase that is observed. However, this assumes that all of the dissipated energy contributes to the luminosity. If part of the energy remains within the star, the radiated energy would be smaller. On the other hand, however, the energy that may be trapped in sub-photospheric layers could trigger a temporary increase in the stellar radius which would then lead to even larger tidal perturbations. Such processes would be interesting to analyze in the future.

Based on the results of our grid of models discussed in the first part of the paper, we are led to conclude that MACHO 80.7443.1718's unusually strong periastron effect is due to its highly super-synchronous rotation rate ($\beta_0 \sim 1.95$), a state that is not expected to be very common in binary systems if they have had time to pseudosynchronize. MACHO 80.7443.1718 belongs to the Lucke-Hodge 58 association which has an estimated age of only a couple of million years (Garmany et al. 1994), which could explain why it still is in such rapid rotation. It is also interesting to note that its β_0 value exceeds the limit $\beta_{crit} = 18/11$ at which the eccentricity tends to increase over time instead of decrease (Zahn 2008).

Our model for MACHO 80.7443.1718 does not predict a dip in the brightness, whereas its observed light curve does show such a dip. MacLeod & Loeb (2023) suggested that the dip could be due to obscuration caused by ejected material. It is tempting to speculate that the steep surface angular velocity gradients and fast bulge radius increase that take place around periastron could trigger brief mass-shedding events. In this respect, a determination of the mass-loss rates at different orbital phases would be most useful.

The effect of tidal shear energy dissipation is often neglected when considering the structure of binary stars and their observational properties. This neglect is due to gaps in our understanding of the dissipation processes that are active and the assumption that viscous shear energy dissipation is negligible in stars.⁸ However, if it is non-negligible, as we assume in this paper, it

can have a significant effect on the stellar properties which, in eccentric systems, become strongly orbital phase-dependent.

Acknowledgements. We thank Werner Schmutz for a critical reading of this paper and the anonymous referee who provided thoughtful comments and suggestions. GK is grateful to the Astronomy Department of the Indiana University for hosting a sabbatical visit during which the research in this paper was concluded. This work was supported by UNAM-PAPIIT 105723.

References

- Alcock, C., Allsman, R. A., Alves, D., et al. 1997, *ApJ*, 486, 697
 Astoul, A., Park, J., Mathis, S., Baruteau, C., & Gallet, F. 2021, *A&A*, 647, A144
 Barker, A. J. & Astoul, A. A. V. 2021, *MNRAS*, 506, L69
 Baruteau, C. & Rieutord, M. 2013, *Journal of Fluid Mechanics*, 719, 47
 Caleo, A., Balbus, S. A., & Tognelli, E. 2016, *MNRAS*, 460, 338
 Dewberry, J. W. & Wu, S. C. 2024, *MNRAS*, 527, 2288
 Efroginsky, M. 2018, *Icarus*, 300, 223
 Eggleton, P. P., Kiseleva, L. G., & Hut, P. 1998, *ApJ*, 499, 853
 Elliott, J. R., Miesch, M. S., & Toomre, J. 2000, *ApJ*, 533, 546
 Estrella-Trujillo, D., Arthur, S. J., Koenigsberger, G., & Moreno, E. 2023, *A&A*, 670, A44
 Fellay, L., Dupret, M. A., & Rosu, S. 2024, arXiv e-prints, arXiv:2401.02573
 Fuller, J. 2017, *MNRAS*, 472, 1538
 Garaud, P. & Kulenthirajah, L. 2016, *ApJ*, 821, 49
 Garmany, C. D., Massey, P., & Parker, J. W. 1994, *AJ*, 108, 1256
 Goldreich, P. & Nicholson, P. D. 1989, *ApJ*, 342, 1079
 Guo, Z. 2020, in *Stars and their Variability Observed from Space*, ed. C. Neiner, W. W. Weiss, D. Baade, R. E. Griffin, C. C. Lovekin, & A. F. J. Moffat, 203–207
 Guo, Z., Shporer, A., Hambleton, K., & Isaacson, H. 2020, *ApJ*, 888, 95
 Hambleton, K., Degroote, P., Conroy, K., et al. 2013, in *EAS Publications Series*, Vol. 64, *EAS Publications Series*, ed. K. Pavlovski, A. Tkachenko, & G. Torres, 285–294
 Harrington, D., Koenigsberger, G., Moreno, E., & Kuhn, J. 2009, *ApJ*, 704, 813
 Harrington, D., Koenigsberger, G., Olgún, E., et al. 2016, *A&A*, 590, A54
 Hirschi, R. & Maeder, A. 2010, *A&A*, 519, A16
 Hut, P. 1981, *A&A*, 99, 126
 Hutchings, J. B. 1979, in *Mass Loss and Evolution of O-Type Stars*, ed. P. S. Conti & C. W. H. De Loore, Vol. 83, 3–20
 Jayasinghe, T., Kochanek, C. S., Strader, J., et al. 2021, *MNRAS*, 506, 4083
 Jayasinghe, T., Stanek, K. Z., Kochanek, C. S., et al. 2020, *MNRAS*, 491, 13
 Jayasinghe, T., Stanek, K. Z., Kochanek, C. S., et al. 2019, *MNRAS*, 489, 4705
 Kämpylä, P. J., Rheinhardt, M., Brandenburg, A., & Kämpylä, M. J. 2020, *A&A*, 636, A93
 Kirk, B., Conroy, K., Prša, A., et al. 2016, *AJ*, 151, 68
 Koenigsberger, G. & Moreno, E. 2016, *Rev. Mexicana Astron. Astrofis.*, 52, 113
 Koenigsberger, G., Moreno, E., & Langer, N. 2021, *A&A*, 653, A127
 Kołaczek-Szymański, P. A., Pigulski, A., Michalska, G., Moździerski, D., & Różański, T. 2021, *A&A*, 647, A12
 Kołaczek-Szymański, P. A., Pigulski, A., Wrona, M., Ratajczak, M., & Udalski, A. 2022, *A&A*, 659, A47
 Kumar, P., Ao, C. O., & Quataert, E. J. 1995, *ApJ*, 449, 294
 Lai, D. 1997, *ApJ*, 490, 847
 Landau, L. D. & Lifshitz, E. M. 1987, *Fluid Mechanics*
 Le Bars, M., Barik, A., Burmann, F., et al. 2022, *Surveys in Geophysics*, 43, 229
 Lee, U. 2017, *MNRAS*, 468, 1864
 Lurie, J. C., Vyhmeister, K., Hawley, S. L., et al. 2017, *AJ*, 154, 250
 MacLeod, M. & Loeb, A. 2023, *Nature Astronomy*, 7, 1218
 Maeder, A. & Meynet, G. 1996, *A&A*, 313, 140
 Maeder, A. & Meynet, G. 2000, *ARA&A*, 38, 143
 Mathis, S., Auclair-Desrotour, P., Guenel, M., Gallet, F., & Le Poncin-Lafitte, C. 2016, *A&A*, 592, A33
 Mathis, S., Palacios, A., & Zahn, J. P. 2004, *A&A*, 425, 243
 McMillan, S. L. W., McDermott, P. N., & Taam, R. E. 1987, *ApJ*, 318, 261
 Moreno, E. & Koenigsberger, G. 1999, *Rev. Mexicana Astron. Astrofis.*, 35, 157
 Moreno, E., Koenigsberger, G., & Harrington, D. M. 2011, *A&A*, 528, 48
 Moreno, E., Koenigsberger, G., & Toledano, O. 2005, *A&A*, 437, 641
 Ogilvie, G. I. 2014, *ARA&A*, 52, 171
 Orosz, J. A. & Hauschildt, P. H. 2000, *A&A*, 364, 265
 Pablo, H., Richardson, N. D., Fuller, J., et al. 2017, *MNRAS*, 467, 2494
 Palate, M., Koenigsberger, G., Rauw, G., Harrington, D., & Moreno, E. 2013a, *A&A*, 556, A49
 Palate, M., Rauw, G., Koenigsberger, G., & Moreno, E. 2013b, *A&A*, 552, A39
 Penev, K., Sasselov, D., Robinson, F., & Demarque, P. 2007, *ApJ*, 655, 1166
 Pérez-de-Tejada, H. 1999, *ApJ*, 525, L65
 Pigulski, A. 2018, in *XXXVIII Polish Astronomical Society Meeting*, ed. A. Róćkańska, Vol. 7, 151–156

⁸ This process, however, plays a major role in celestial objects such as Jupiter's moons Io and Europa and most likely play a role in close-in exoplanets.

- Press, W. H. & Teukolsky, S. A. 1977, *ApJ*, 213, 183
- Richard, D. & Zahn, J.-P. 1999, *A&A*, 347, 734
- Richardson, N. D., Pablo, H., Sterken, C., et al. 2018, *MNRAS*, 475, 5417
- Savonije, G. J., Papaloizou, J. C. B., & Albers, F. 1995, *MNRAS*, 277, 471
- Scharlemann, E. T. 1981, *ApJ*, 246, 292
- Schenk, A. K., Arras, P., Flanagan, É. É., Teukolsky, S. A., & Wasserman, I. 2001, *Phys. Rev. D*, 65, 024001
- Shi, X., Wen, D., Bao, X., Li, C., & Huang, Y. 2006, *Science China Earth Sciences*, 49, 492
- Sterken, C. & Breysacher, J. 1997, *A&A*, 328, 269
- Sun, M., Townsend, R. H. D., & Guo, Z. 2023, *ApJ*, 945, 43
- Symon, K. R. 1971, *Mechanics* (Addison-Wesley)
- Talon, S., Zahn, J. P., Maeder, A., & Meynet, G. 1997, *A&A*, 322, 209
- Terquem, C. 2021, *MNRAS*, 503, 5789
- Thompson, S. E., Everett, M., Mullanly, F., et al. 2012, *ApJ*, 753, 86
- Tkachenko, A., Matthews, J. M., Aerts, C., et al. 2016, *MNRAS*, 458, 1964
- Toledano, O., Moreno, E., Koenigsberger, G., Detmers, R., & Langer, N. 2007, *A&A*, 461, 1057
- Townsend, R. H. D. & Sun, M. 2023, *ApJ*, 953, 48
- van Genderen, A. M. & Sterken, C. 2007, *Information Bulletin on Variable Stars*, 5782, 1
- Zahn, J. P. 1975, *A&A*, 41, 329
- Zahn, J. P. 1977, *A&A*, 57, 383
- Zahn, J. P. 1992, *A&A*, 265, 115
- Zahn, J. P. 2008, in *EAS Publications Series*, Vol. 29, *EAS Publications Series*, ed. M. J. Goupil & J. P. Zahn, 67–90

Table 3. Eccentric models.

Num	β_0	V_{rot}	$\langle \dot{E}_{tot} \rangle$	\dot{E}_{tot}^{per}	\dot{E}_{tot}^{ap}	$\Delta\dot{E}/L_*$
P=6.0 e=0.1 $r_{per}=32.15$						
201	0.20	11	$7.60 \cdot 10^{-1}$	1.65	$4.10 \cdot 10^{-1}$	$3.10 \cdot 10^{-3}$
202	0.40	22	$2.30 \cdot 10^{-1}$	$5.40 \cdot 10^{-1}$	$1.20 \cdot 10^{-1}$	$1.05 \cdot 10^{-3}$
203	0.60	34	$4.80 \cdot 10^{-2}$	$1.40 \cdot 10^{-1}$	$2.00 \cdot 10^{-2}$	$3.00 \cdot 10^{-4}$
204	0.80	45	$4.20 \cdot 10^{-3}$	$1.20 \cdot 10^{-2}$	$1.20 \cdot 10^{-3}$	$2.70 \cdot 10^{-5}$
205	0.88	49	$2.50 \cdot 10^{-3}$	$4.80 \cdot 10^{-3}$	$2.00 \cdot 10^{-3}$	$7.00 \cdot 10^{-6}$
206	0.95	53	$4.20 \cdot 10^{-3}$	$2.40 \cdot 10^{-3}$	$5.50 \cdot 10^{-3}$	$-7.75 \cdot 10^{-6}$
207	1.00	56	$8.80 \cdot 10^{-3}$	$3.40 \cdot 10^{-3}$	$1.10 \cdot 10^{-2}$	$-1.90 \cdot 10^{-5}$
208	1.05	59	$1.50 \cdot 10^{-2}$	$7.10 \cdot 10^{-3}$	$2.00 \cdot 10^{-2}$	$-3.22 \cdot 10^{-5}$
209	1.20	67	$6.30 \cdot 10^{-2}$	$4.90 \cdot 10^{-2}$	$7.60 \cdot 10^{-2}$	$-6.75 \cdot 10^{-5}$
210	1.40	79	$2.70 \cdot 10^{-1}$	$2.70 \cdot 10^{-1}$	$3.00 \cdot 10^{-1}$	$-7.50 \cdot 10^{-5}$
211	1.60	90	$9.30 \cdot 10^{-1}$	$9.30 \cdot 10^{-1}$	$8.80 \cdot 10^{-1}$	$1.25 \cdot 10^{-4}$
212	1.88	105	3.01	3.48	3.12	$9.00 \cdot 10^{-4}$
213	1.95	109	4.20	4.84	4.32	$1.30 \cdot 10^{-3}$
P=8.73 e=0.3 $r_{per}=32.1$						
301	0.20	12	$6.50 \cdot 10^{-1}$	2.47	$1.80 \cdot 10^{-1}$	$5.73 \cdot 10^{-3}$
302	0.40	24	$1.80 \cdot 10^{-1}$	$6.90 \cdot 10^{-1}$	$3.50 \cdot 10^{-2}$	$1.64 \cdot 10^{-3}$
303	0.60	37	$4.90 \cdot 10^{-2}$	$2.30 \cdot 10^{-1}$	$1.00 \cdot 10^{-2}$	$5.50 \cdot 10^{-4}$
304	0.80	49	$2.40 \cdot 10^{-2}$	$7.90 \cdot 10^{-2}$	$1.10 \cdot 10^{-2}$	$1.70 \cdot 10^{-4}$
305	0.88	54	$1.60 \cdot 10^{-2}$	$1.70 \cdot 10^{-2}$	$9.60 \cdot 10^{-3}$	$1.85 \cdot 10^{-5}$
306	0.95	58	$1.30 \cdot 10^{-4}$	$7.60 \cdot 10^{-3}$	$1.30 \cdot 10^{-2}$	$-1.35 \cdot 10^{-5}$
307	1.00	61	$2.20 \cdot 10^{-2}$	$6.70 \cdot 10^{-3}$	$1.60 \cdot 10^{-2}$	$-2.33 \cdot 10^{-5}$
308	1.05	64	$2.40 \cdot 10^{-2}$	$5.60 \cdot 10^{-3}$	$1.70 \cdot 10^{-2}$	$-2.85 \cdot 10^{-5}$
309	1.20	73	$5.30 \cdot 10^{-2}$	$3.00 \cdot 10^{-2}$	$3.60 \cdot 10^{-2}$	$-1.50 \cdot 10^{-5}$
310	1.40	86	$1.70 \cdot 10^{-1}$	$2.10 \cdot 10^{-1}$	$1.20 \cdot 10^{-1}$	$2.25 \cdot 10^{-4}$
311	1.60	98	$6.00 \cdot 10^{-1}$	$9.50 \cdot 10^{-1}$	$4.80 \cdot 10^{-1}$	$1.17 \cdot 10^{-3}$
312	1.88	115	4.42	5.60	3.64	$4.90 \cdot 10^{-3}$
313	1.95	119	6.45	8.11	5.53	$6.43 \cdot 10^{-3}$
P=14.49 e=0.5 $r_{per}=32.1$						
501	0.20	13	$5.40 \cdot 10^{-1}$	2.83	3.62	$-1.97 \cdot 10^{-3}$
502	0.40	26	$2.20 \cdot 10^{-1}$	1.04	$3.00 \cdot 10^{-2}$	$2.52 \cdot 10^{-3}$
503	0.60	39	$1.30 \cdot 10^{-1}$	$4.30 \cdot 10^{-1}$	$6.00 \cdot 10^{-2}$	$9.25 \cdot 10^{-4}$
504	0.80	52	$4.30 \cdot 10^{-2}$	$9.00 \cdot 10^{-2}$	$2.00 \cdot 10^{-2}$	$1.75 \cdot 10^{-4}$
507	1.00	66	$2.40 \cdot 10^{-2}$	$1.10 \cdot 10^{-2}$	$4.72 \cdot 10^{-3}$	$1.57 \cdot 10^{-5}$
508	1.05	69	$2.50 \cdot 10^{-2}$	$8.93 \cdot 10^{-3}$	$5.53 \cdot 10^{-3}$	$8.50 \cdot 10^{-6}$
509	1.10	72	$2.80 \cdot 10^{-2}$	$1.03 \cdot 10^{-2}$	$6.76 \cdot 10^{-3}$	$8.85 \cdot 10^{-6}$
510	1.20	78	$3.90 \cdot 10^{-2}$	$3.01 \cdot 10^{-2}$	$8.38 \cdot 10^{-3}$	$5.43 \cdot 10^{-5}$
511	1.40	92	$1.10 \cdot 10^{-1}$	$2.40 \cdot 10^{-1}$	$3.09 \cdot 10^{-2}$	$5.23 \cdot 10^{-4}$
512	1.60	105	$4.30 \cdot 10^{-1}$	1.13	$1.60 \cdot 10^{-1}$	$2.43 \cdot 10^{-3}$
513	1.88	123	4.65	8.18	3.55	$1.16 \cdot 10^{-2}$
514	1.95	128	8.80	13.2	7.42	$1.44 \cdot 10^{-2}$
P=31.17 e=0.7 $r_{per}=32.15$						
701	0.20	14	$3.60 \cdot 10^{-1}$	3.07	$4.96 \cdot 10^{-3}$	$7.66 \cdot 10^{-3}$
702	0.40	28	$2.00 \cdot 10^{-1}$	1.40	$3.86 \cdot 10^{-2}$	$3.40 \cdot 10^{-3}$
703	0.60	42	$1.20 \cdot 10^{-1}$	$5.10 \cdot 10^{-1}$	$5.89 \cdot 10^{-2}$	$1.13 \cdot 10^{-3}$
704	0.80	56	$4.70 \cdot 10^{-2}$	$1.20 \cdot 10^{-1}$	$1.12 \cdot 10^{-2}$	$2.72 \cdot 10^{-4}$
707	1.00	70	$2.20 \cdot 10^{-2}$	$2.43 \cdot 10^{-2}$	$3.02 \cdot 10^{-3}$	$5.32 \cdot 10^{-5}$
708	1.05	73	$2.06 \cdot 10^{-2}$	$2.09 \cdot 10^{-2}$	$2.87 \cdot 10^{-3}$	$4.51 \cdot 10^{-5}$
709	1.10	77	$2.05 \cdot 10^{-2}$	$2.40 \cdot 10^{-2}$	$2.69 \cdot 10^{-3}$	$5.33 \cdot 10^{-5}$
711	1.40	98	$6.90 \cdot 10^{-2}$	$4.20 \cdot 10^{-1}$	$1.11 \cdot 10^{-2}$	$1.02 \cdot 10^{-3}$
712	1.60	112	$3.00 \cdot 10^{-1}$	2.21	$8.33 \cdot 10^{-2}$	$5.32 \cdot 10^{-3}$
713	1.88	131	3.71	16.2	2.24	$3.49 \cdot 10^{-2}$
714	1.95	136	5.66	22.6	3.70	$4.72 \cdot 10^{-2}$

Notes. Surface equatorial rotation velocity V_{rot} is in km/s; total energy dissipation rate averaged over the orbital cycle, total energy dissipation rate at periastron and at apastron are in units of 10^{35} ergs/s. The last column gives $(\dot{E}_{tot}^{per} - \dot{E}_{tot}^{ap})/L_*$ where $L_*=4.\times 10^{37}$ ergs/s is the adopted total luminosity for a 10_\odot star such as the one we model. A negative value occurs when the brightness at apastron is greater than at periastron. The heading for each set models lists the corresponding orbital period in days, eccentricity, and orbital separation at periastron R_{per} in solar units.

Table 4. Circular orbit set.

Model	β_0	V_{rot}	$\langle \dot{E}_{tot} \rangle$	$\Delta \dot{E}/L_*$
P=6 d, e=0				
102	0.40	18	0.24	6.0×10^{-4}
103	0.60	27	4.2×10^{-2}	1.0×10^{-4}
104	0.80	36	5.8×10^{-3}	1.4×10^{-5}
106	0.95	43	7.9×10^{-5}	2.0×10^{-7}
108	1.05	48	6.8×10^{-5}	1.7×10^{-7}
109	1.20	55	4.3×10^{-3}	1.1×10^{-5}
111	1.60	73	0.17	4.3×10^{-4}
113	1.95	89	0.92	2.3×10^{-3}

Notes. Surface equatorial rotation velocity V_{rot} is given in km/s; total energy dissipation rate averaged over the orbital cycle in units of 10^{35} ergs/s.

Table 5. Input parameters and results MACHO 80.7443.1718.

Parameter	Value	Notes
Data from observations and input parameters		
P_{orb}	32.83627 d	(a)
e	0.507	(a)
m_1	34.5 M_\odot	(b)
m_2	15.7 M_\odot	(b)
R_1	23.7 R_\odot	(b)
V_{rot}	250 km/s	(c)
L_*	1.57×10^{39} ergs/	(b)
$\Delta F_{peri}/F$	$\sim 23\%$	(d)
β_0	1.95	
λ	1	
N_{cy}	100	
N_r	5	
a	159 R_\odot	
r_{per}	78.5 R_\odot	
Output values and results		
\dot{E}_{peri}	3.7×10^{38} ergs/s	(e)
\dot{E}_{apo}	6.6×10^{36} ergs/s	(e)
$\langle \dot{E}_{tot} \rangle$	6.5×10^{37} ergs/s	(e)
$\Delta \dot{E}_{peri}/L_*$	23.5%	(f)
$R_{max-peri}$	23.83 R_\odot	(g)
$R_{min-per}$	23.63 R_\odot	(g)
R_{max-ap}	23.76 R_\odot	(g)
R_{min-ap}	23.66 R_\odot	(g)
$\langle R_{peri} \rangle$	23.71 R_\odot	(h)
$\langle R_{ap} \rangle$	23.70 R_\odot	(h)

Notes. (a) Jayasinghe et al. (2019); (b) Jayasinghe et al. (2021); (c) Adopting an orbital inclination $i=44^\circ$ and $v \sin(i)=174$ km/s from Jayasinghe et al. (2021); (d) estimated from Fig. 9 of Jayasinghe et al. (2021) which shows maximum light at levels of ~ 1.2 to ~ 1.26 (depending on the TESS sector) above the average value ~ 1 between subsequent periastron passages. ; (e) Output from TIDES-nvv; (f) $(\dot{E}_{tot}^{peri} - \dot{E}_{tot}^{apo})/L_*$; (g) Maximum and minimum equatorial radius at periastron and apastron, including high frequency oscillations, from the TIDES-1 version of the code with $\nu=0.028 R_\odot^2/d$. The corresponding values from the TIDES1-vv model with $\lambda=0.01$ are 23.76 and 23.67 R_\odot . (h) average polar radius at periastron and apastron from the TIDES-1 version of the code.

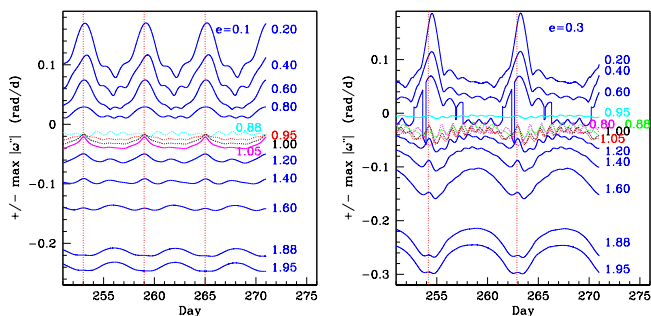


Fig. A.1. Maximum perturbation of the surface angular velocity at the equator plotted as a function of time for $e=0.1$ (left) and $e=0.3$ (right). The velocity is measured in the rest reference frame of the rotating star. Positive values indicate motion in the direction of the orbital motion, negative values to motion opposite to the orbital motion. Vertical lines indicate times of periastron. Each curve is labeled with its value of β_0 . The smallest tidal perturbations for $e=0.1$ occur for $\beta_0=0.88$. For $e=0.3$, the $\beta_0=0.80, 0.88, 1.00$ and 1.05 curves show low amplitude oscillations and are very similar. The smallest perturbations are observed for $\beta_0=0.95$. Observational perspective: Surface layer is rotating faster than the inner core for $\beta_0 < 1$ and rotating slower in $\beta_0 > 1$ models. Also, these stars are likely to display variations in the shape of the photospheric line profiles as discussed in Moreno et al. (2005) and Harrington et al. (2009, 2016). TEOs are evident mostly for $\beta_0 \sim 1$ models.

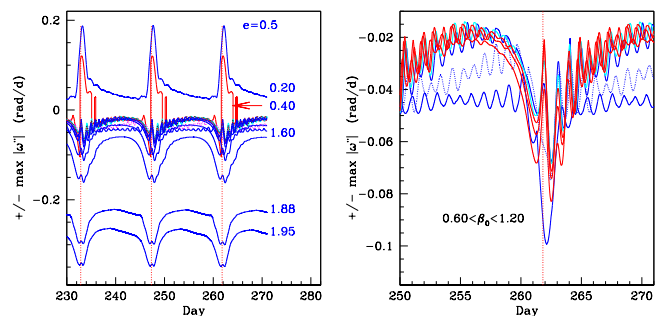


Fig. A.2. Maximum perturbation of the surface angular velocity at the equator for $e=0.5$ plotted as a function of time. The velocity is measured in the reference frame at rest in the rotating star. Positive values indicate motion in the direction of the orbital motion, negative values motion opposite to the orbital motion. Vertical lines indicate times of periastron. *Left:* All models with β_0 increasing from top to bottom. Models close to pseudosynchronism are not labeled for clarity in the figure. *Right:* Models with $0.60 \leq \beta_0 \leq 1.00$ are plotted in blue and cyan and those with $1.05 \leq \beta_0 \leq 1.20$ in red.

Appendix A: Extremum value of the angular velocity at each timestep

The eccentric binary models all display a variability pattern in the tidal perturbations on the orbital timescale, the largest amplitudes occurring around the time of periastron. We quantify the time-dependent perturbations at each computational timestep by finding the largest deviation of the angular velocity from the underlying rigidly rotating core at each computational time step. We define this quantity as $\max(|\omega(r, \theta, \varphi, t)|)$, where ω is the instantaneous angular velocity of the volume element located at (r, θ, φ) at time t as measured in the reference frame that rotates with the primary star. Once this quantity is located at each timestep of the computation, it is assigned a positive or negative sign depending on whether this maximum velocity is in the direction of the orbital motion or in the opposite direction. The first case occurs mostly in the subsynchronous models ($\beta_0 < 1$) where the tidal force acts to increase the velocity toward corotation. The second case occurs in the supersynchronous models where the tidal force acts to slow the velocity down. This general behavior is illustrated in Fig. A.1 for $e=0.1$ and 0.3 models and Fig. A.2 for $e=0.5$.

Around the time of periastron, the perturbation becomes strongest and the angular velocity changes rapidly creating either a maximum (subsynchronous systems) or a minimum peak (highly supersynchronous systems). Systems with rotation speeds that are not very far from corotation at periastron tend to present high frequency oscillations throughout the orbital cycle and a variety of behaviors at periastron.

Some of the models show a maximum peak at periastron and negative values at other phases (for example, $e=0.3, \beta_0=0.60$ and $e=0.5, \beta_0=0.40$) but in general have either positive or negative values throughout the orbit.

Table A.1. Turbulent viscosity ten layer models.

Model	β_0	V_{rot}	$\langle \dot{E}_{tot} \rangle$	$\log \langle \nu / R_\odot^2 / d \rangle$									
				Periastron					Apastron				
				k=2	k=4	k=6	k=8	k=10	k=2	k=4	k=6	k=8	k=10
				$e=0.1$		$P=6$ d							
201	0.20	11	7.61e-1	-3.20	-2.86	-2.72	-2.29	-1.17	-3.20	-2.89	-2.72	-2.78	-1.96
202	0.40	22	2.26e-1	-3.60	-3.03	-2.86	-2.43	-1.36	-3.59	-3.03	-2.84	-2.97	-1.94
203	0.60	34	4.78e-2	-3.81	-3.33	-3.02	-2.62	-1.50	-4.18	-3.32	-3.02	-3.12	-2.28
204	0.80	45	4.19e-3	-3.80	-3.95	-3.64	-2.92	-1.81	-4.59	-4.20	-3.64	-3.37	-1.97
205	0.88	49	2.48e-3	-3.87	-4.35	-3.66	-3.12	-1.91	-4.76	-4.50	-3.81	-3.21	-1.87
206	0.95	53	4.19e-3	-3.84	-4.04	-3.36	-3.33	-2.10	-4.74	-4.06	-3.36	-3.09	-1.83
207	1.00	56	8.78e-3	-3.85	-3.78	-3.21	-3.26	-2.21	-4.85	-3.78	-3.21	-2.99	-1.78
208	1.05	59	1.48e-2	-3.86	-3.56	-3.12	-3.17	-2.35	-4.61	-3.55	-3.12	-2.93	-1.73
209	1.20	67	6.32e-2	-3.86	-3.19	-2.94	-2.96	-1.96	-4.10	-3.19	-2.94	-2.79	.161
210	1.40	79	2.69e-1	-3.44	-2.95	-2.78	-2.67	-1.61	-3.43	-2.95	-2.78	-2.64	-1.47
211	1.60	90	8.33e-1	-3.12	-2.81	-2.68	-2.49	-1.40	-3.11	-2.81	-2.68	-2.52	-1.36
212	1.88	105	3.01	-2.88	-2.66	-2.56	-2.29	-1.18	-2.88	-2.66	-2.57	-2.36	-1.18
213	1.95	109	4.20	-2.83	-2.63	-2.54	-2.25	-1.12	-2.83	-2.63	-2.54	-2.32	-1.13
				$e=0.3$		$P=8.73$ d							
301	0.20	13	6.61e-1	-3.55	-3.02	-2.83	-2.14	-1.09	-3.54	-3.02	-2.85	-2.77	-1.61
302	0.40	27	1.81e-1	-4.16	-3.42	-3.12	-2.29	-1.27	-4.15	-3.42	-3.12	-3.14	-1.70
303	0.60	40	5.28e-2	-4.22	-3.85	-3.35	-2.46	-1.35	-4.40	-4.14	-3.73	-3.24	-1.63
304	0.80	53	2.47e-2	-4.29	-3.88	-3.26	-2.66	-1.51	-4.40	-3.88	-3.26	-3.29	-1.49
305	0.88	59	1.58e-2	-4.46	-3.88	-3.30	-2.90	-1.75	-4.54	-3.86	-3.30	-3.23	-1.40
306	0.95	63	4.21e-4	-4.37	-4.42	-4.00	-3.92	-2.40	-4.55	-4.21	-3.73	-3.81	-1.30
307	1.00	67	2.34e-2	-4.47	-3.61	-3.18	-3.32	-2.02	-4.44	-3.60	-3.18	-3.03	-1.32
308	1.05	70	2.66e-2	-4.48	-3.56	-3.16	-3.43	-2.13	-4.27	-3.55	-3.16	-2.98	-1.29
309	1.20	80	5.80e-2	-4.25	-3.32	-3.03	-2.97	-1.86	-4.26	-3.32	-3.03	-2.96	-1.22
310	1.40	93	2.02e-1	-3.74	-3.06	-2.86	-2.62	-1.53	-3.72	-3.06	-2.86	-2.84	-1.14
311	1.60	107	7.18e-1	-3.21	-2.85	-2.70	-2.41	-1.31	-3.20	-2.85	-2.70	-2.69	-1.11
312	1.88	125	4.36	-2.80	-2.60	-2.49	-2.21	-1.09	-2.80	-2.60	-2.49	-2.52	-1.14
313	1.95	130	6.45	-2.75	-2.56	-2.46	-2.17	-1.03	-2.75	-2.56	-2.46	-2.44	-1.10
				$e=0.0$ $P=6$ d									
102	0.40	18	1.83e-1	-3.23	-3.04	-2.96	-2.74	-1.62					
103	0.60	27	3.79e-2	-4.20	-3.29	-3.00	-2.88	-1.79					
104	0.80	36	6.01e-3	-4.09	-3.53	-3.34	-3.22	-2.10					
106	0.95	43	2.09e-4	-4.28	-4.31	-3.96	-3.76	-2.70					
108	1.05	48	1.41e-3	-4.65	-4.43	-3.93	-3.80	-2.70					
109	1.20	55	4.13e-3	-4.22	-3.86	-3.30	-3.16	-2.10					
111	1.60	73	1.52e-1	-3.67	-3.04	-2.84	-2.73	-1.61					
113	1.95	89	9.27e-1	-3.12	-2.81	-2.68	-2.51	-1.38					

Notes. V_{rot} is the initial equatorial rotation velocity in units of km/s; \dot{E}_{tot} is the total energy dissipation rate after the numerical simulation has evolved to 50 orbital periods in units of 10^{35} ergs/s; ν is the viscosity as computed in the model using Eq. 2 with $\lambda=1$ in units of R_\odot^2/d . k indicates the layer with $k=1$ the layer adjoining the core and $k=10$ the surface layer, each layer having a depth of $\Delta R=0.329 R_\odot$. The header of each set of model grids indicates the corresponding orbital period and eccentricity.

